



# Enhanced hydrological cycle increases ocean heat uptake and moderates transient climate change

Maofeng Liu<sup>1</sup>✉, Gabriel Vecchi<sup>2,3</sup>, Brian Soden<sup>1</sup>, Wenchang Yang<sup>2</sup> and Bosong Zhang<sup>1</sup>

**The large-scale moistening of the atmosphere in response to increasing greenhouse gases amplifies the existing patterns of precipitation minus evaporation ( $P - E$ ), which, in turn, amplifies the spatial contrast in sea surface salinity. Here, by performing a series of transient  $\text{CO}_2$  doubling experiments, we demonstrate that surface salinification driven by the amplified dry conditions ( $P - E < 0$ ), primarily in the subtropical ocean, accelerates ocean heat uptake. The salinification also drives the sequestration of upper-level heat into the deeper ocean, reducing the thermal stratification and increasing the heat uptake through positive feedback. The change in Atlantic Meridional Overturning Circulation due to salinification has a secondary role in heat uptake. Consistent with the heat uptake changes, the transient climate response would increase by approximately 0.4 K without this process. Observed multidecadal changes in subsurface temperature and salinity resemble those simulated, indicating that anthropogenically forced changes in salinity are probably enhancing ocean heat uptake.**

The increased concentration of atmospheric greenhouse gases has reduced the longwave cooling of the Earth's climate system to space, resulting in planetary warming, which works to eventually bring the climate towards a new—warmer—equilibrium<sup>1</sup>. It has been estimated that over 90% of the top-of-atmosphere (TOA) energy imbalance is captured by the ocean as increased ocean heat content (OHC)<sup>2,3</sup>. The resulting upper ocean warming can enhance the thermal stratification of the ocean<sup>4</sup> and therefore act to dampen mode water formation<sup>5</sup>. A recent study<sup>2</sup> summarizing observation-based OHC estimates<sup>6–11</sup> and climate model simulations from the Coupled Model Intercomparison Project Phase 5 (CMIP5)<sup>12–15</sup> claims a stronger rate of ocean warming over the period of 2005–2017 ( $0.54\text{--}0.64\text{ W m}^{-2}$ ) relative to the period of 1971–2010 ( $0.36\text{--}0.39\text{ W m}^{-2}$ ). Furthermore, in both observationally constrained OHC data<sup>16</sup> and climate model simulations<sup>17</sup>, a substantial portion of increased OHC is found in tropics and subtropics (that is, towards the Equator from  $40^\circ$  latitude). This creates a conundrum—given the stably stratified low-latitude ocean, how does the warming water get subducted to produce subtropical ocean heat uptake despite further stabilization from upper-ocean warming<sup>4,18</sup>?

We propose that the amplification of the spatial pattern of sea surface salinity (SSS)<sup>19–23</sup> resulting from the enhancement of the global hydrological cycle<sup>24</sup> provides an important supporting mechanism for the rate of ocean heat uptake. A robust consequence of anthropogenic warming is the increase in atmospheric moisture content controlled by the Clausius–Clapeyron (CC) relationship, leading to the strengthening of the water cycle expressed as the amplification of the existing patterns of surface freshwater fluxes ( $P - E$ )<sup>24</sup>. The enhancement of  $P - E$  amplifies the mean state, that is, “wet regions get wetter and dry regions drier”<sup>24</sup>. As SSS in part reflects large-scale patterns of  $P - E$ , the enhancement of the global hydrological cycle acts to amplify patterns of SSS: ‘fresh gets fresher and salty gets saltier’<sup>19,20,25,26</sup>. Analyses of long-term observations of SSS have revealed that the spatial changes of SSS largely resemble the climatological SSS distribution<sup>19</sup>. We hypothesize that salinification of the subtropical surface ocean provides an important buoyancy sink that helps to compensate for the stabilizing impact of upper ocean warming

and enhance low-latitude heat uptake, and the enhancement of the hydrological cycle therefore moderates the transient climate change.

In this Article, we quantify the impact of sea-surface salinification on ocean heat uptake and transient climate warming using a global coupled ocean–atmosphere climate model (the Forecast-oriented Low Ocean Resolution version of the Coupled Model version 2.5 (FLOR)) developed at the Geophysical Fluid Dynamics Laboratory<sup>17,27</sup>. We conducted a suite of transient  $\text{CO}_2$  doubling experiments in which the atmospheric  $\text{CO}_2$  concentration is increased by 1% per year until doubling. The experiments include a baseline run using the standard configuration of FLOR (labelled STD) and a perturbation run using a modified FLOR in which the SSS is nudged to the seasonally varying control climatology from the STD run on global scales (labelled fixed-SSS-GL; Methods). Differences in the  $\text{CO}_2$  response between these two configurations highlight the influences of SSS changes on transient climate warming.

Compared with the STD configuration, the fixed-SSS-GL version shows a greater increase in the global mean surface temperature with a larger transient climate response (TCR) by 0.4 K, highlighting the role of  $\text{CO}_2$ -induced SSS changes in reducing the rate of surface warming in response to  $\text{CO}_2$  doubling (Fig. 1). The mean difference (0.002 K) in annual global mean surface temperature between the 100-year STD and fixed-SSS-GL control runs is three orders of magnitude smaller than the difference in TCR, suggesting that fixing SSS has a relatively small climatological effect on unforced simulations of surface temperature (Supplementary Text 1 and Supplementary Fig. 1).

Given the similar climate feedback parameter ( $-1.6$  and  $-1.5\text{ W m}^{-2}\text{ K}^{-1}$  for the STD and fixed-SSS-GL version, respectively; Methods, Supplementary Text 2 and Supplementary Fig. 2), the greater surface warming in the fixed-SSS-GL experiment relative to the STD run should result in a larger radiative response of the climate system. On the basis of the TOA energy balance ( $R(t) = Q(t) + \lambda \Delta T(t)$ , where  $R$  is the net radiation at the TOA,  $Q$  is the radiative forcing,  $\lambda$  is the climate feedback parameter,  $\Delta T$  is the surface warming and  $t$  is time), a lower radiative imbalance at the TOA occurs when SSS is fixed given the same  $\text{CO}_2$ -induced radiative forcing (Fig. 2a). This

<sup>1</sup>Rosenstiel School of Marine and Atmospheric Science, University of Miami, Miami, FL, USA. <sup>2</sup>Department of Geosciences, Princeton University, Princeton, NJ, USA. <sup>3</sup>Princeton Environmental Institute, Princeton University, Princeton, NJ, USA. ✉e-mail: [maofengliu2012@gmail.com](mailto:maofengliu2012@gmail.com)

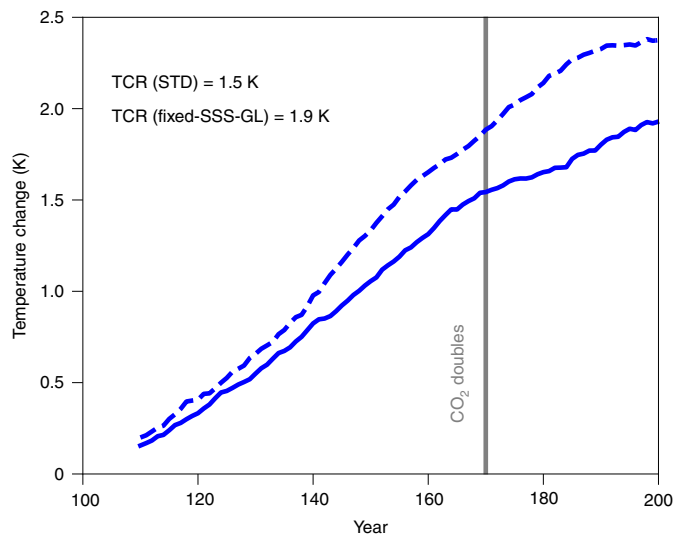


**Fig. 1 | The response of surface temperature to transient CO<sub>2</sub> forcing.**

Time series of global mean surface temperature changes (in K) in response to a 1% annual increase in CO<sub>2</sub> concentration for the STD (solid line) and fixed-SSS-GL (dashed line) configurations. Data are plotted as the 20-year running mean.

indicates that the fixed-SSS-GL version has a much lower ocean heat-uptake efficiency<sup>28,29</sup>, defined as the ratio of net radiation at the TOA to the global surface temperature increase. Consistent with this, the fixed-SSS-GL experiment shows a smaller increase in OHC compared with the STD experiment (Fig. 2a). Similar to global mean surface temperature, there is a relatively small effect of fixing SSS on control simulations of net radiation at the TOA and OHC (Supplementary Text 1 and Supplementary Fig. 3).

The STD version shows a greater increase in ocean heat uptake in response to the CO<sub>2</sub> forcing relative to the fixed-SSS-GL version

(Fig. 2b). The greatest increase occurs in the tropical and subtropical Atlantic Ocean and the second greatest increase occurs in the subtropical South Pacific (Fig. 2b), broadly mirroring regions in which SSS shows the largest increase<sup>30</sup> (Fig. 2c). The results support our hypothesis on the role of sea surface salinification in enhancing heat penetration into the deeper ocean by reduced density stratification resulting from upper-ocean warming. In response to the CO<sub>2</sub> forcing, the fixed-SSS-GL run shows a greater heat-equivalent buoyancy flux than the STD run, which is partially attributed to freshwater flux (Supplementary Fig. 4), further demonstrating the role of surface salinification in enhancing the buoyancy sink. The spatial distribution of SSS change in response to the CO<sub>2</sub> forcing (Fig. 2c) is broadly consistent with the change in  $P-E$  (Fig. 2d) strongly tied to the mean state (Supplementary Fig. 5), echoing the impact of the amplified water cycle on surface salinity changes<sup>19–21,24</sup>.

However, we noticed regions with mismatch between the OHC and SSS. First, the extension of the positive OHC anomaly in the subtropical southeastern Pacific to the western Pacific convective region (Fig. 2b) is not seen in the SSS pattern (Fig. 2c). This mismatch is primarily driven by the climatological oceanic transport towards the convective zone (Supplementary Fig. 6a–c); the change in ocean circulation is secondary (Supplementary Fig. 6d–f). Second, the enhanced OHC anomaly in the subtropical North Atlantic over South Atlantic is not observed in the SSS. The underlying reason will be addressed later in the discussion of the impact of ocean circulation.

Relative to the fixed-SSS-GL version, the STD version exhibits deeper warming (Fig. 3a)—a reduced increase of heating within the upper 300 m, in agreement with the reduced increase of surface temperature (Fig. 1). The downward shift in OHC arising from SSS changes is further evident in the zonally integrated subsurface temperature in response to CO<sub>2</sub> doubling (Fig. 3c,e). Note that, relative to the zonal mean, the zonal integral provides a more relevant measure to compare tropics and subpolar regions by taking into account the difference in area per unit latitude at different latitudes related to both the convergence of meridians and differences in land mass. The Atlantic Ocean accounts for 54% of all heat increase, and its

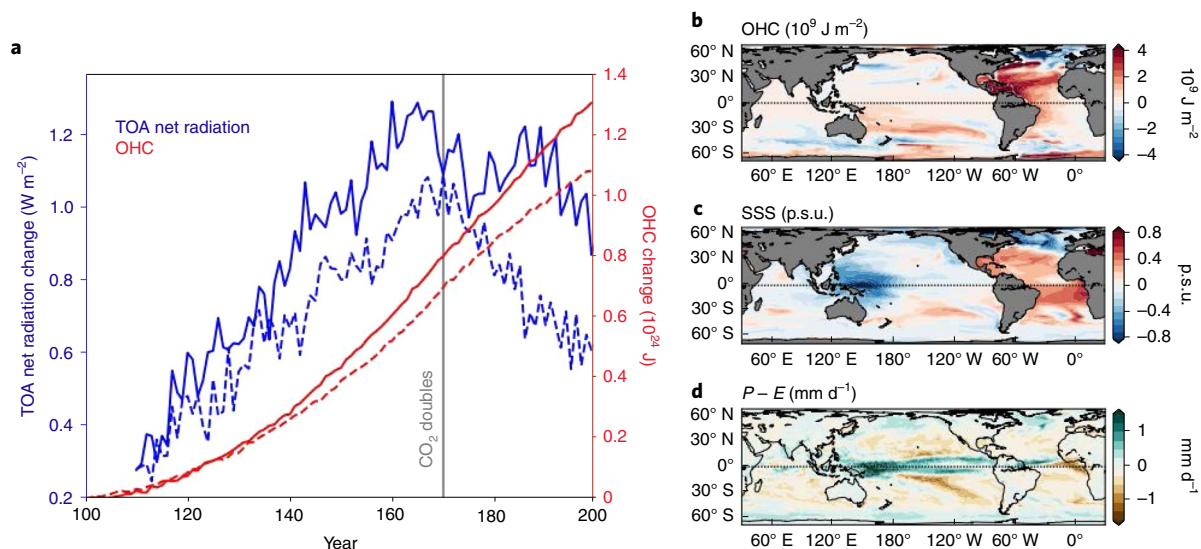


**Fig. 2 | The impact of fixed SSS on the response of OHC and TOA net radiation to CO<sub>2</sub> forcing.** **a**, Annual series of changes in TOA net radiation ( $\text{W m}^{-2}$ ; blue) and OHC ( $10^{24} \text{ J}$ ; red) in response to a 1% annual increase in CO<sub>2</sub> for the STD (solid line) and fixed-SSS-GL (dashed line) version. The grey line indicates year 170 when the CO<sub>2</sub> doubles. The TOA net radiation is plotted as 10-year running mean. **b**, The difference in the response of OHC ( $10^9 \text{ J m}^{-2}$ ) to CO<sub>2</sub> doubling between the STD and fixed-SSS-GL version. The response was computed using years 161–180 from the CO<sub>2</sub> run and years 101–200 from the control run. **c**, The difference in the response of SSS (practical salinity unit (p.s.u.)) to CO<sub>2</sub> doubling between the STD and fixed-SSS-GL version. The response was computed using years 161–180 from the CO<sub>2</sub> run and years 101–200 from the control run. **d**, The response of  $P-E$  ( $\text{mm d}^{-1}$ ) pattern to CO<sub>2</sub> doubling for the STD version.

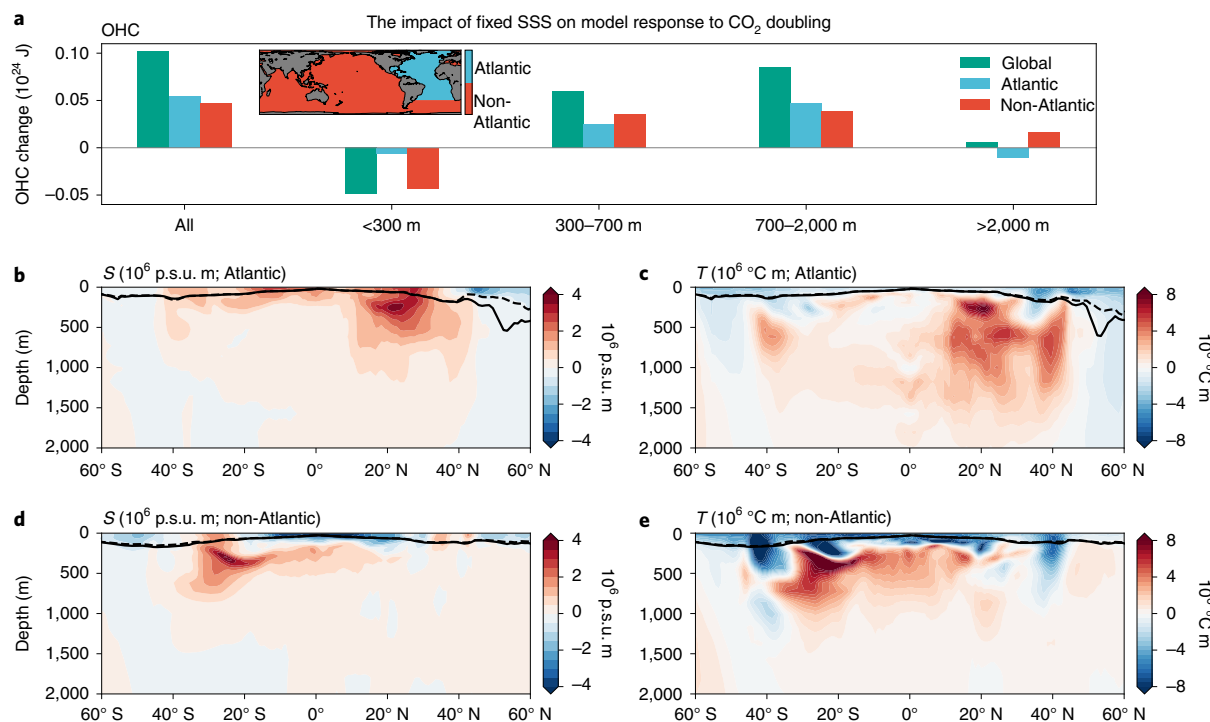


**Fig. 3 | The impact of fixed SSS on the model response to CO<sub>2</sub> doubling.** **a**, The difference in the response of OHC ( $10^{24}$  J) to transient CO<sub>2</sub> doubling between the STD and fixed-SSS-GL version as a function of ocean depth. The response was computed using years 161–180 from the CO<sub>2</sub> run and years 101–200 from the control run. Inset: the area of Atlantic and non-Atlantic Ocean for computing total OHC. **b,c**, The difference in the response of zonal-integral ocean salinity ( $S$ ; **b**;  $10^6$  p.s.u. m; colour) and ocean temperature ( $T$ ; **c**;  $10^6$  °C m; colour) between the STD and fixed-SSS-GL version in the Atlantic using the same period as in **a**. **d,e**, The difference in the response of zonal-integral ocean salinity (**d**;  $10^6$  p.s.u. m; colour) and ocean temperature (**e**;  $10^6$  °C m; colour) between the STD and fixed-SSS-GL version in non-Atlantic ocean using the same period as in **a**. The black lines in **b–d** indicate the winter mixed layer depth (mld; m) from the control runs (solid) and CO<sub>2</sub> runs (dashed), respectively. The mld is defined as the depth at which the density difference with respect to the surface level is greater than or equal to  $0.03 \text{ kg m}^{-3}$ . The mld values in **b** and **d** are from the STD version and the mld values in **c** and **e** are from the fixed-SSS-GL version.

greatest salinity-induced increase of subsurface temperature occurs in the northern subtropics where the increase of subsurface salinity also reaches its peak (Fig. 3b,c). For ocean basins other than the Atlantic, there is also correspondence between the positive anomaly of subsurface temperature and salinity as shown in the southern subtropics (Fig. 3d,e), primarily in the Pacific Ocean (Supplementary Fig. 7b,c). Although the Indian Ocean shows a much smaller magnitude than the Pacific, the positive salinity anomaly (for example, around 20°S) corresponds with upper-level cooling and deeper ocean warming (Supplementary Fig. 7d,e). These results suggest that increased subsurface salinity in the subtropical ocean driven by surface salinification plays an important role of in modulating the vertical distribution of heat through accelerated heat uptake. A consequence of heat sequestration from the upper level to deeper ocean is the decrease in the upper-level thermal stratification (Fig. 4e,f), which further increases the heat uptake through positive feedback. The lower thermal stratification in the fixed-SSS-GL run relative to the STD run makes a considerable contribution to the total difference in the upper ocean stratification (Fig. 4a,b), highlighting the important role of this feedback in amplifying the salinification-driven reduction in stratification (Fig. 4c,d).

The wind-driven turbulent mixing in the upper layers seems to have a less important role in the difference in OHC response between the two versions: (1) the mixed layer depth in winter shows insignificant difference between the two versions of FLOR in the subtropical ocean; (2) most of the extra heat sink is sequestered deeper than the mixed layer depth (Fig. 3c,e). The intermediate layer (700–2,000 m) sequesters more heat than the other layers (Fig.

3a), in part driven by the increased heat penetration that is associated with the positive salinity anomaly (Fig. 3b,d). The confinement of this salinity anomaly within the upper 1,000 m (Fig. 3b,d) implies that other mechanisms (which are discussed below) are needed to cause the extra increase in heat in the lower portion of the intermediate layer.

Given the importance of ocean circulation in driving heat transport and related temperature changes, we further investigated the role of ocean circulation. Weakening of the Atlantic Meridional Overturning Circulation (AMOC) in response to greenhouse gas forcing, as seen in a number of previous studies<sup>32–34</sup>, is seen in the idealized CO<sub>2</sub> doubling experiments with FLOR (Supplementary Fig. 8). The fixed-SSS-GL version produces less weakening of the AMOC relative to the STD run, probably due to the suppression of the subpolar freshening by climatological SSS nudging<sup>33</sup>. The greater AMOC weakening in the STD version results in a reduction in northward transport of warm water towards the subpolar North Atlantic and therefore more heat storage in the subtropics compared with the fixed-SS-GL version, which helps to explain why the enhanced OHC anomaly in the North Atlantic (Fig. 2c) is not seen in SSS (Fig. 2d).

The impact of the difference in the AMOC change was further examined using another set of experiments that nudge SSS only in the subtropical Atlantic (labelled fixed-SSS-subAtl; Supplementary Fig. 9) to enable subpolar freshening. The fixed-SSS-subAtl version produced a similar AMOC weakening relative to the STD run, enabling us to distinguish the relative role of the AMOC and salinification on OHC changes. In response to the CO<sub>2</sub> forcing, the STD

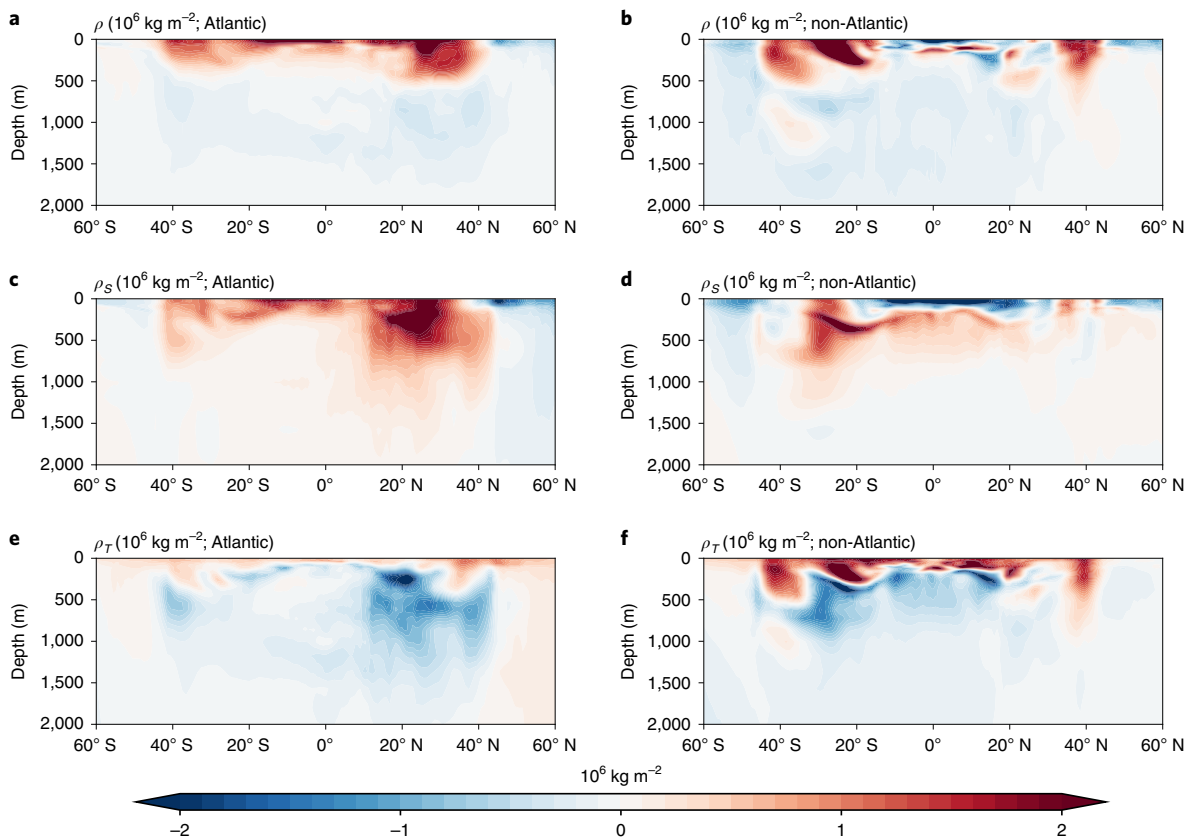


**Fig. 4 | The impact of fixed SSS on the response of ocean stratification to CO<sub>2</sub> doubling. a,b**, The difference in the response of zonal-integral ocean density ( $\rho$ ;  $10^6 \text{ kg m}^{-2}$ ) between the STD and fixed-SSS-GL version for Atlantic (**a**) and non-Atlantic Ocean (**b**). The response was computed using years 161–180 from the CO<sub>2</sub> run and years 101–200 from the control run. **c,d**, The contribution of salinity to the difference in density change ( $\rho_S$ ;  $10^6 \text{ kg m}^{-2}$ ) between the STD and fixed-SSS-GL version for Atlantic (**c**) and non-Atlantic Ocean (**d**). **e,f**, The contribution of temperature to the difference in density change ( $\rho_T$ ;  $10^6 \text{ kg m}^{-2}$ ) between the STD and fixed-SSS-GL version for Atlantic (**e**) and non-Atlantic Ocean (**f**). For **a–f**, the response was computed using years 161–180 from the CO<sub>2</sub> run and years 101–200 from the control run.

version shows a greater increase in OHC by  $4.1 \times 10^{22} \text{ J}$  relative to the fixed-SSS-subAtl version in the Atlantic Ocean (Supplementary Fig. 10a). This accounts for 74% of the increase in OHC relative to the fixed-SSS-GL version, resulting from the competition between a greater OHC increase in subpolar Atlantic and a smaller OHC increase at lower latitudes (Supplementary Fig. 11 versus Fig. 2b). This meridional difference in OHC increase is partially attributed to the difference in AMOC weakening between the fixed-SSS-subAtl and fixed-SSS-GL version. By contrast, the greater weakening of the AMOC in the fixed-SSS-subAtl relative to the fixed-SSS-GL version causes increased salinity at lower latitudes due to reduced northward transport (Supplementary Fig. 12) and therefore enhances ocean heat uptake. The heat anomaly between the STD and fixed-SSS-subAtl version in the subtropical North Atlantic overlaps with the positive salt anomaly (Supplementary Fig. 10b,c), further implying the key role of salinification in accelerating heat uptake. Furthermore, the heat anomaly is primarily sequestered in the upper ocean ( $<700 \text{ m}$ ) (Supplementary Fig. 10c) in contrast to the intermediate level (700–2,000 m) for the heat anomaly between the STD and fixed-SSS-GL version (Fig. 3). These results suggest the role of ocean circulation in heat sequestration below the upper ocean for the following reasons. First, the enhanced northward transport of salty water in the fixed-SSS-GL version relative to the fixed-SSS-subAtl experiment due to less AMOC weakening could lead to decreased salt in the subtropics (Supplementary Fig. 12) and therefore reduced heat sink to deeper levels. Second, the enhanced southward import of North Atlantic Deep Water in the

fixed-SSS-GL version could transport more subpolar cold water to the intermediate level in the subtropics, resulting in less warming compared with in the other two experiments.

In addition to fixed-SSS-subAtl, we conducted another set of experiments that partially nudged SSS in non-Atlantic ocean basins (labelled fixed-SSS-nonAtl; Supplementary Fig. 13). The fixed-SSS-nonAtl version shows a lesser weakening of the AMOC than the fixed-SSS-subAtl version, probably due to the subtropical Atlantic salinification driven by enhanced hydrological drying (Fig. 2d). The sea water with enhanced salinity moves northwards, leading to a lower ocean stratification in the subpolar region and a stronger AMOC. However, the weakening of the AMOC in the fixed-SSS-nonAtl version is closer to the STD version than the fixed-SSS-GL version, resulting in a reduced impact from the AMOC on OHC changes (Supplementary Fig. 8). Outside of the Atlantic, the fixed-SSS-nonAtl version exhibits similar changes in OHC and subsurface temperature (Supplementary Fig. 14a,e) to the fixed-SSS-GL version (Fig. 3a,e), which is dominated by the Pacific Ocean (Supplementary Fig. 15a,e). The correspondence between salinity and temperature in the subtropics further demonstrates the important role of salinification in enhancing ocean heat uptake.

We compared the simulated model response with observations to explore the impact of increased CO<sub>2</sub> on the current climate change. The linear trend of SSS from an observational dataset spanning the period of 1968–2017 from National Centers for Environmental Information (NCEI)<sup>16</sup> resembles the spatial pattern of SSS change seen in the idealized FLOR experiments (Supplementary Fig. 16a),



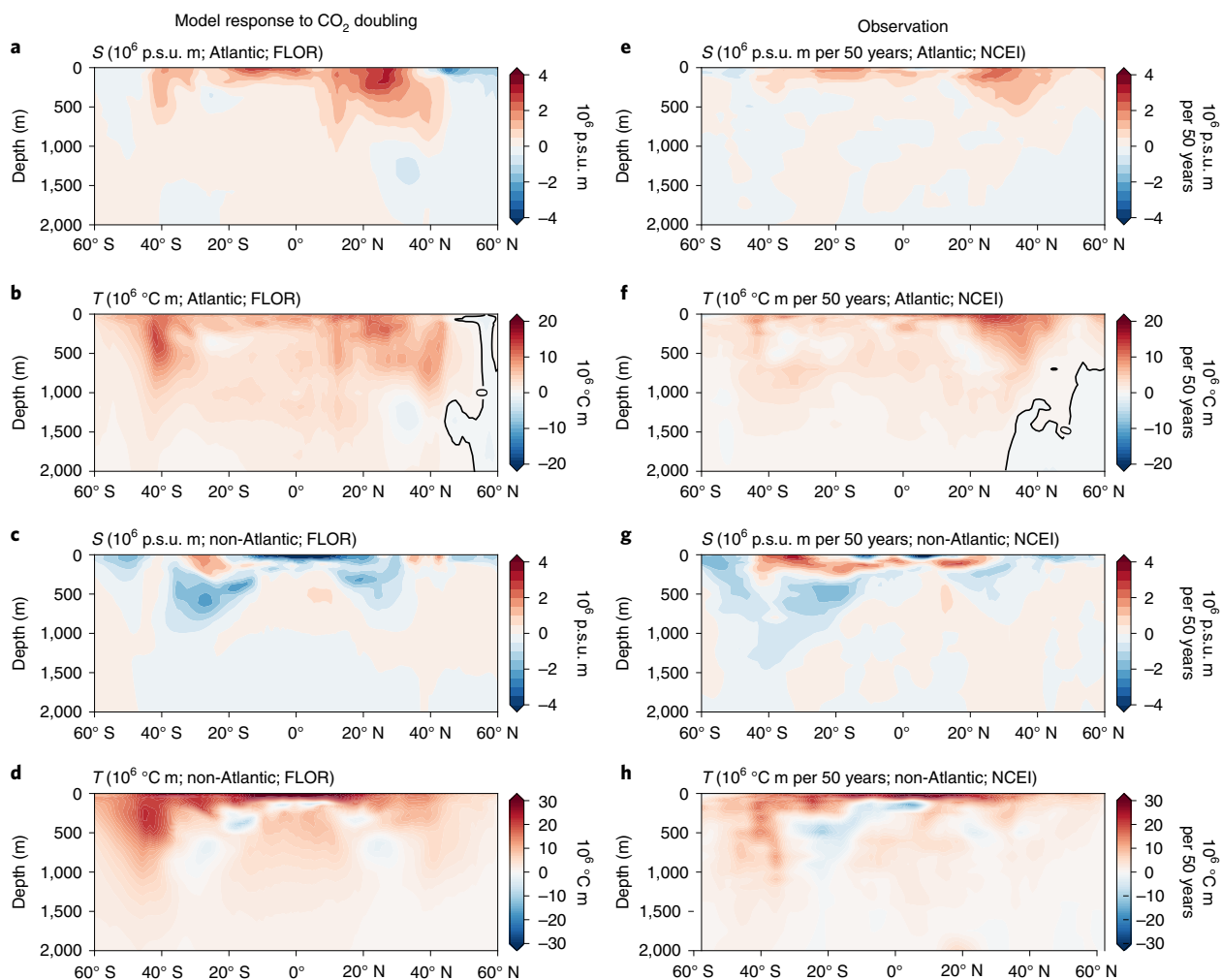


**Fig. 5 | Comparison between FLOR model experiments and observations.** **a,b**, The change in zonal-integral ocean subsurface salinity (**a**;  $10^6$  p.s.u. m; colour) and ocean temperature (**b**;  $10^6$  °C m; colour) in response to transient  $\text{CO}_2$  doubling in the Atlantic Ocean for the STD runs. **c,d**, The change in zonal-integral ocean subsurface salinity (**c**;  $10^6$  p.s.u. m; colour) and ocean temperature (**d**;  $10^6$  °C m; colour) in response to transient  $\text{CO}_2$  doubling in non-Atlantic Ocean for the STD runs. The response was computed using years 161–180 from the  $\text{CO}_2$  run and years 101–200 from the control run. **e–h**, The linear trend of ocean salinity (**e,g**;  $10^6$  p.s.u. m per 50 years) and temperature (**f,h**;  $10^6$  °C m per 50 years) in the Atlantic Ocean (**e,f**) and non-Atlantic Ocean (**g,h**) from the NCEI data over the period of 1968–2017. The trend is tuned by the ratio of  $\text{CO}_2$  concentration at  $\text{CO}_2$  doubling in FLOR to that in 2017 from observations.

a resemblance that is robust across different observationally based ocean salinity datasets (Supplementary Fig. 16b–d), suggesting the emergent signal of human-induced forcing in shaping the observed changes of ocean salinity, as identified by a number of recent studies<sup>22,30,31</sup>. The similarity is not seen in the subpolar North Atlantic, where SSS shows an increase in FLOR, while there is a decrease in observations. The underlying reason will be discussed later.

Similar to SSS, the simulated response of ocean subsurface temperature and salinity to the idealized  $\text{CO}_2$  forcing from the STD version also resembles many key features in the linear trend of observations spanning the period of 1968–2017 (Fig. 5), implying the likely emergent signal of human-induced forcing in driving the temperature and salinity changes<sup>22,30,31,35</sup>. This similarity is broadly robust across datasets (Supplementary Figs. 17–19).

In the Atlantic Ocean, both the STD simulations and in situ data show a positive salt anomaly (Fig. 5a,e) overlapped with the heat anomaly (Fig. 5b,f) in the subtropics which, as demonstrated in the FLOR experiments, is primarily driven by subtropical surface salinification associated with intensified hydrological cycle. Similar to SSS (Fig. 2c versus Supplementary Fig. 16), a major difference

lies in the subpolar North Atlantic where the decrease in the subsurface salinity and temperature in FLOR, especially in the upper ocean, is less clear in observations, primarily driven by their difference in AMOC changes. AMOC weakening in response to  $\text{CO}_2$  forcing in the standard FLOR experiment (Supplementary Fig. 8) is not seen in the past few decades due to strong decadal variability<sup>36,37</sup>, although recent studies using proxy data claimed the century-scale weakening of the AMOC<sup>38,39</sup>.

For ocean basins other than the Atlantic, both the STD simulations and observations show a decreased salinity in the upper ocean extending to 1,000 m in subtropics (Fig. 5c,g), broadly overlapping with the regions with cooling (Fig. 5d,h). Although the surface salinification in the south subtropics from the STD version does not exceed the rate of freshening beneath (Fig. 5c), it leads to more salt and heat penetration into deeper layers than the fixed-SSS-GL version in which the surface salinification is suppressed (Fig. 3d,e). The 40°–50° S zone of the Southern Ocean shows substantial warming (Fig. 5b,d), which was claimed in a recent study<sup>40</sup> to result from the northward heat transport that is associated with the Antarctic Circumpolar Current.

Here we highlight the previously overlooked role of subtropical salinification—driven by the enhanced water cycle<sup>19–24</sup> in response to greenhouse warming—in accelerating the rate of ocean heat uptake and therefore moderating transient climate warming. Performing a set of climate model experiments, we found that the largest enhancement in ocean heat uptake occurs in the subtropical South Pacific and the tropical and subtropical Atlantic Ocean, where SSS shows the greatest increase. The results also highlight the role of salinification in modulating the vertical distribution of subsurface temperature by sequestering upper-level heat to deeper ocean, which could lead to a reduced thermal stratification and further enhance ocean heat uptake through a positive feedback. Without the surface salinification, the FLOR experiments suggest that the TCR could increase by 0.4 K, close to the standard deviation of TCR from the CMIP6 models<sup>41</sup>. This suggests that the multimodel spread in transient climate sensitivity may be partially traced to their spread in simulating ocean salinity. The increasing emergence of the anthropogenic signal in the ocean water masses<sup>35</sup> raises the need for future research of the competing mechanism between upper ocean warming and subtropical salinification in ocean stratification, which is critical for an improved understanding of past and future ocean heat uptake and transient climate change.

### Online content

Any methods, additional references, Nature Research reporting summaries, source data, extended data, supplementary information, acknowledgements, peer review information; details of author contributions and competing interests; and statements of data and code availability are available at <https://doi.org/10.1038/s41558-021-01152-0>.

Received: 19 November 2020; Accepted: 12 August 2021;

Published online: 23 September 2021

### References

- Mitchell, J. F. B., Manabe, S., Meleshko, V. & Tokioka, T. in *IPCC Climate Change: The IPCC Scientific Assessment* (eds Houghton, J. T., Jenkins, G. J. & Ephraums, J. J.) (Cambridge Univ. Press, 1990).
- Cheng, L., Abraham, J., Hausfather, Z. & Trenberth, K. E. How fast are the oceans warming? *Science* **363**, 128–129 (2019).
- Trenberth, K. E., Fasullo, J. T. & Balmaseda, M. A. Earth's energy imbalance. *J. Clim.* **27**, 3129–3144 (2014).
- Li, G. et al. Increasing ocean stratification over the past half-century. *Nat. Clim. Chang.* **10**, 1116–1123 (2020).
- Stevens, S. W., Johnson, R. J., Maze, G. & Bates, N. R. A recent decline in North Atlantic subtropical mode water formation. *Nat. Clim. Chang.* **10**, 335–341 (2020).
- Ishii, M. et al. Accuracy of global upper ocean heat content estimation expected from present observational data sets. *Sola* **13**, 163–167 (2017).
- Cheng, L. et al. Improved estimates of ocean heat content from 1960 to 2015. *Sci. Adv.* **3**, e1601545 (2017).
- Domingues, C. M. et al. Improved estimates of upper-ocean warming and multi-decadal sea-level rise. *Nature* **453**, 1090–1093 (2008).
- Abraham, J. P. et al. A review of global ocean temperature observations: implications for ocean heat content estimates and climate change. *Rev. Geophys.* **51**, 450–483 (2013).
- von Schuckmann, K. et al. Heat stored in the Earth system: where does the energy go? *Earth Syst. Sci. Data* **12**, 2013–2041 (2020).
- Meyssignac, B. et al. Measuring global ocean heat content to estimate the earth energy imbalance. *Front. Mar. Sci.* **6**, 432 (2019).
- Taylor, K. E., Stouffer, R. J. & Meehl, G. A. An overview of CMIP5 and the experiment design. *Bull. Am. Meteorol. Soc.* **93**, 485–498 (2012).
- Larson, E. J. L., Portmann, R. W., Solomon, S. & Murphy, D. M. Decadal attribution of historic temperature and ocean heat content change to anthropogenic emissions. *Geophys. Res. Lett.* **47**, e2019GL085905 (2020).
- Bronselaer, B. & Zanna, L. Heat and carbon coupling reveals ocean warming due to circulation changes. *Nature* **584**, 227–233 (2020).
- Bilbao, R. A. F., Gregory, J. M., Bonttes, N., Palmer, M. D. & Stott, P. Attribution of ocean temperature change to anthropogenic and natural forcings using the temporal, vertical and geographical structure. *Clim. Dyn.* **53**, 5389–5413 (2019).
- Levitus, S. et al. World ocean heat content and thermosteric sea level change (0–2000 m), 1955–2010. *Geophys. Res. Lett.* **39**, L10603 (2012).
- Vecchi, G. A. et al. Tropical cyclone sensitivities to CO<sub>2</sub> doubling: roles of atmospheric resolution, synoptic variability and background climate changes. *Clim. Dyn.* **53**, 5999–6033 (2019).
- Capotondi, A., Alexander, M. A., Bond, N. A., Curchitser, E. N. & Scott, J. D. Enhanced upper ocean stratification with climate change in the CMIP3 models. *J. Geophys. Res. Oceans* **117**, C04031 (2012).
- Durack, P. J. & Wijffels, S. E. Fifty-year trends in global ocean salinities and their relationship to broad-scale warming. *J. Clim.* **23**, 4342–4362 (2010).
- Durack, P. J., Wijffels, S. E. & Matear, R. J. Ocean salinities reveal strong global water cycle intensification during 1950 to 2000. *Science* **336**, 455–458 (2012).
- Skirris, N. et al. Salinity changes in the World Ocean since 1950 in relation to changing surface freshwater fluxes. *Clim. Dyn.* **43**, 709–736 (2014).
- Terray, L. et al. Near-surface salinity as nature's rain gauge to detect human influence on the tropical water cycle. *J. Clim.* **25**, 958–977 (2012).
- Lago, V. et al. Simulating the role of surface forcing on observed multidecadal upper-ocean salinity changes. *J. Clim.* **29**, 5575–5588 (2016).
- Held, I. M. & Soden, B. J. Robust responses of the hydrological cycle to global warming. *J. Clim.* **19**, 5686–5699 (2006).
- IPCC *Climate Change 2013: The Physical Science Basis* (eds Stocker, T. F. et al.) (Cambridge Univ. Press, 2013).
- Bindoff, N. L. et al. *IPCC Special Report on the Ocean and Cryosphere in a Changing Climate* 477–587 (IPCC, 2019).
- Vecchi, G. A. et al. On the seasonal forecasting of regional tropical cyclone activity. *J. Clim.* **27**, 7994–8016 (2014).
- Gregory, J. M. & Mitchell, J. F. B. The climate response to CO<sub>2</sub> of the Hadley Centre coupled AOGCM with and without flux adjustment. *Geophys. Res. Lett.* **24**, 1943–1946 (1997).
- Raper, S. C. B., Gregory, J. M. & Stouffer, R. J. The role of climate sensitivity and ocean heat uptake on AOGCM transient temperature response. *J. Clim.* **15**, 124–130 (2002).
- Stott, P. A., Sutton, R. T. & Smith, D. M. Detection and attribution of Atlantic salinity changes. *Geophys. Res. Lett.* **35**, L21702 (2008).
- Pierce, D. W., Gleckler, P. J., Barnett, T. P., Santer, B. D. & Durack, P. J. The fingerprint of human-induced changes in the ocean's salinity and temperature fields. *Geophys. Res. Lett.* **39**, 2–7 (2012).
- Stouffer, R. J. et al. Investigating the cause of the response of the thermohaline circulation to past and future climate changes. *J. Clim.* **19**, 1365–1387 (2006).
- Liu, W., Fedorov, A. V., Xie, S.-P. & Hu, S. Climate impacts of a weakened Atlantic Meridional Overturning Circulation in a warming climate. *Sci. Adv.* **6**, eaaz4876 (2020).
- Levang, S. J. & Schmitt, R. W. What causes the AMOC to weaken in CMIP5? *J. Clim.* **33**, 1535–1545 (2019).
- Silvy, Y., Guilyardi, E., Sallée, J.-B. & Durack, P. J. Human-induced changes to the global ocean water masses and their time of emergence. *Nat. Clim. Chang.* **10**, 1030–1036 (2020).
- Robson, J., Ortega, P. & Sutton, R. A reversal of climatic trends in the North Atlantic since 2005. *Nat. Geosci.* **9**, 513–517 (2016).
- Jackson, L. C., Peterson, K. A., Roberts, C. D. & Wood, R. A. Recent slowing of Atlantic overturning circulation as a recovery from earlier strengthening. *Nat. Geosci.* **9**, 518–522 (2016).
- Thornalley, D. J. R. et al. Anomalous weak Labrador Sea convection and Atlantic overturning during the past 150 years. *Nature* **556**, 227–230 (2018).
- Caesar, L., Rahmstorf, S. & Feulner, G. On the relationship between Atlantic meridional overturning circulation slowdown and global surface warming. *Environ. Res. Lett.* **15**, 24003 (2020).
- Armour, K. C., Marshall, J., Scott, J. R., Donohoe, A. & Newsom, E. R. Southern Ocean warming delayed by circumpolar upwelling and equatorward transport. *Nat. Geosci.* **9**, 549–554 (2016).
- Meehl, G. A. et al. Context for interpreting equilibrium climate sensitivity and transient climate response from the CMIP6 Earth system models. *Sci. Adv.* **6**, eaba1981 (2020).

**Publisher's note** Springer Nature remains neutral with regard to jurisdictional claims in published maps and institutional affiliations.

© The Author(s), under exclusive licence to Springer Nature Limited 2021

## Methods

**Model experiments.** We used the Forecast-oriented Low Ocean Resolution model (FLOR)<sup>27,42</sup> developed at the Geophysical Fluid Dynamics Laboratory (GFDL). FLOR has a horizontal resolution of approximately 50 km for the atmosphere and land components developed from GFDL Coupled Model (CM) version 2.5 and a coarser (~1°) resolution for the oceanic and sea ice components from GFDL CM version 2.1. We used the FLOR model to conduct a set of fully coupled experiments. The first experiment was labelled as a standard control simulation in which the radiative forcing and land use/land cover is maintained as the level of year 1990 for 200 years. The first 100 years were treated as model spin-up and discarded from further analyses. As well as the standard control simulation, we also performed three control experiments in which the SSS of the fully coupled model was nudged to the climatological SSS over the global ocean (labelled fixed-SSS-GL), the subtropical Atlantic Ocean (Supplementary Fig. 9; labelled fixed-SSS-subAtl) and non-Atlantic ocean basins (Supplementary Fig. 13; labelled fixed-SSS-nonAtl) using model year 101 in the standard control simulation for the initial condition. Corresponding to each standard control simulation, we conducted a perturbation experiment in which the atmospheric CO<sub>2</sub> concentration was increased at a rate of 1% per year until doubling from year 101 (that is, 100 years after model initialization), and was then held fixed. For each experiment, the climate response to CO<sub>2</sub> doubling was computed as difference between model year 161–180 from the perturbation run and model year 101–200 from the control run.

**Radiative feedback computations.** We used the radiative kernel method<sup>43</sup> to calculate the transient radiative feedbacks for the CO<sub>2</sub> stabilization period (that is, year 161–180). The radiative kernel for a feedback variable  $x$  is defined as  $K^* = \partial R / \partial x$ , where  $R$  is the net TOA flux and  $x$  is an individual radiative state variable (for example, temperature, water vapour, clouds or surface albedo). The radiative kernel was derived from CloudSat/CALIPSO measurements<sup>44,45</sup>.

**OHC analysis.** The OHC is computed as follows:

$$\text{OHC} = \int_{x_1}^{x_2} \int_{y_1}^{y_2} \int_{z_1}^{z_2} \rho C_p T dx dy dz \quad (1)$$

where  $\rho$  is the density of sea water,  $C_p$  is the specific heat capacity,  $T$  is the temperature,  $x_1$  and  $x_2$  denote the western and eastern boundaries of the ocean,  $y_1$  and  $y_2$  denote the southern and northern boundaries, and  $z_1$  and  $z_2$  denote the range of the ocean depth.

**Surface buoyancy flux analysis.** The surface buoyancy flux ( $B$ ) is composed of contributions from both heat ( $B_H$ ) and freshwater flux ( $B_{FW}$ )<sup>46</sup>:

$$B = B_H + B_{FW} = \frac{g}{\rho_0} [(\alpha Q_H / c_p) + \rho_0 \beta S (P - E + R)] \quad (2)$$

where  $g$  is the gravitational acceleration,  $\rho_0$  is a reference density,  $\alpha$  and  $\beta$  are the thermal expansion and saline contraction coefficients, respectively,  $c_p$  is the specific heat capacity of seawater,  $S$  is the SSS,  $Q_H$  is the air–sea heat flux (W m<sup>−2</sup>),  $P$  is precipitation,  $E$  is evaporation and  $R$  is runoff into the ocean. For a more convenient comparison, both the buoyancy and freshwater flux are expressed as heat-equivalent flux, denoted  $Q_B$  and  $Q_{FW}$ , respectively<sup>46</sup>. The heat-equivalent buoyancy flux is:

$$Q_B = Q_H + Q_{FW} = \frac{\rho_0 c_p}{g \alpha} B \quad (3)$$

and the heat-equivalent freshwater flux is:

$$Q_{FW} = \frac{\rho_0 c_p}{g \alpha} B_{FW} \quad (4)$$

**Ocean density analysis.** We decompose the response of ocean density to CO<sub>2</sub> forcing ( $\Delta\rho$ ) by computing the relative contributions from both salinity ( $\Delta\rho_S$ ) and temperature ( $\Delta\rho_T$ ):

$$\Delta\rho = \rho_{\text{CO}_2} - \rho \quad (5)$$

$$\Delta\rho_S = \beta \Delta S \rho \quad (6)$$

$$\Delta\rho_T = -\alpha \Delta T \rho \quad (7)$$

where  $\rho_{\text{CO}_2}$  is the ocean density from years 161–180 in the CO<sub>2</sub> run,  $\rho$  is the ocean density from years 101–200 in the control run,  $\Delta S$  and  $\Delta T$  are the response of salinity and temperature to CO<sub>2</sub> doubling, respectively,  $\beta$  is the haline contraction coefficient and  $\alpha$  is the thermal expansion coefficient.

**Ocean salinity and temperature data.** We used four gridded datasets of ocean salinity and temperature for the period of 1968–2017. The first three datasets constructed on the basis of in situ measurements are from the National Centers

for Environmental Information (NCEI), United States<sup>16</sup>, the Japan Meteorological Agency (JMA), Japan<sup>6</sup>, and the Institute of Atmospheric Physics (IAP), China<sup>47</sup>. We also use an ocean reanalysis product from Ocean Reanalysis System 4 (ORAS4)<sup>48</sup> that constrains the model simulations with in situ measurements. The linear trend of ocean salinity and temperature spanning from 1968 to 2017 was computed using an ordinary least-squares linear fit and then multiplied by 50 to represent changes. Before comparing the trend to FLOR-simulated change, we tuned it roughly by the ratio of CO<sub>2</sub> concentration at CO<sub>2</sub> doubling in FLOR (708 ppm) to that in 2017 (407 ppm) from observations. By extrapolating the trend, we focus on the linear component of the response of subsurface salinity and temperature to the CO<sub>2</sub> forcing. Note that linearity is an important component of the changing trend of observed CO<sub>2</sub> concentrations (Supplementary Fig. 20).

## Data availability

The NCEI ocean salinity and temperature data are available online ([https://www.nodc.noaa.gov/OC5/3M\\_HEAT\\_CONTENT/](https://www.nodc.noaa.gov/OC5/3M_HEAT_CONTENT/)). The JMA data are available online (<https://climate.mri-jma.go.jp/pub/ocean/ts/v7.3/>). The IAP data are available at <http://159.226.119.60/cheng/>. The ORAS4 data are available at <ftp://ftp-icdc.cen.uni-hamburg.de/EASYInit/ORA-S4/>. The input data for running the FLOR experiments presented in this work and processed data for graphics from the four datasets and FLOR model outputs are available at tigris-web at Princeton University ([http://tigris-web.princeton.edu/~maofeng/SSS\\_OHU\\_TCR/data/](http://tigris-web.princeton.edu/~maofeng/SSS_OHU_TCR/data/)).

## Code availability

The climate model used in this study is GFDL FLOR with code available at the NOAA/GFDL website (<https://www.gfdl.noaa.gov/cm2-5-and-flor/>). All graphics were produced using Python v.3.6 (<https://www.python.org/downloads/release/python-360/>). The codes needed to set up the FLOR experiment and Python scripts used for analyses and producing main figures are available at GitHub ([https://github.com/maofeng2012/SSS\\_OHC\\_TCR](https://github.com/maofeng2012/SSS_OHC_TCR); <https://doi.org/10.5281/zenodo.5149277>).

## References

- Jia, L. et al. Improved seasonal prediction of temperature and precipitation over land in a high-resolution GFDL climate model. *J. Clim.* **28**, 2044–2062 (2015).
- Soden, B. J. et al. Quantifying climate feedbacks using radiative kernels. *J. Clim.* **21**, 3504–3520 (2008).
- Zhang, B., Kramer, R. J. & Soden, B. J. Radiative feedbacks associated with the Madden–Julian oscillation. *J. Clim.* **32**, 7055–7065 (2019).
- Kramer, R. J., Matus, A. V., Soden, B. J. & L’Ecuyer, T. S. Observation-based radiative kernels from CloudSat/CALIPSO. *J. Geophys. Res. Atmos.* **124**, 5431–5444 (2019).
- Cerovecki, I., Talley, L. D. & Mazloff, M. R. A Comparison of Southern Ocean air–sea buoyancy flux from an ocean state estimate with five other products. *J. Clim.* **24**, 6283–6306 (2011).
- Cheng, L. et al. Improved estimates of changes in upper ocean salinity and the hydrological cycle. *J. Clim.* **33**, 10357–10381 (2020).
- Balmaseda, M. A., Mogensen, K. & Weaver, A. T. Evaluation of the ECMWF ocean reanalysis system ORAS4. *Q. J. R. Meteorol. Soc.* **139**, 1132–1161 (2013).

## Acknowledgements

This work was supported by award 80NSSC20K0879 from the National Aeronautics and Space Administration and award DE-SC0021333 from the US Department of Energy. The simulations presented in this paper were performed on computational resources managed and supported by Princeton Research Computing at Princeton University.

## Author contributions

B.S., G.V. and M.L. designed the research. G.V., M.L. and W.Y. performed the simulations. M.L. and B.Z. performed the analysis. M.L. wrote the draft. All of the authors contributed to interpreting the results and writing the paper.

## Competing interests

The authors declare no competing interests.

## Additional information

**Supplementary information** The online version contains supplementary material available at <https://doi.org/10.1038/s41558-021-01152-0>.

**Correspondence and requests for materials** should be addressed to Maofeng Liu.

**Peer review information** *Nature Climate Change* thanks Veronique Lago, M. Cameron Rencurrel and the other, anonymous, reviewer(s) for their contribution to the peer review of this work.

**Reprints and permissions information** is available at [www.nature.com/reprints](http://www.nature.com/reprints).